J. Synchrotron Rad. (1996). **3**, 173–184

New Features of Dislocation Images in Third-Generation Synchrotron Radiation Topographs

F. Zontone,[a] L. Mancini,[a] R. Barrett,[a] J. Baruchel,[a] J. Härtwig[a] and Y. Epelboin[b]

[a]*European Synchrotron Radiation Facility, BP 220, F-38043 Grenoble, France, and* [b]*LMCP, UA 009 CNRS, Universités P. M. Curie et D. Diderot, Case 115, 75252 Paris CEDEX 05, France*

(*Received 19 December 1995; accepted 13 February 1996*)

Some aspects of the dislocation contrast observed at third-generation synchrotron radiation set-ups are presented. They can be explained by taking into account angular deviation effects on the beam propagation, which are visible because of the 'almost plane-wave' character of these sources. In particular, we show how the evolution of the direct image width of a dislocation as a function of the sample-to-film distance can allow a complete determination of the Burgers vector, *i.e.* in sign and modulus. In addition, experimental results obtained in monochromatic beam topography are compared with simulated images calculated assuming plane-wave illumination and are demonstrated to show a satisfactory agreement. The utility of the weak-beam technique in enhancing the spatial resolution is demonstrated and a criterion for the selection of experimental conditions depending upon the required spatial resolution, signal-to-noise ratio and exposure time is presented.

Keywords: topography; dislocations; direct images; simulations; X-ray coherence; image contrast.

1. Introduction

Synchrotron radiation diffraction topography is a well established imaging technique for the investigation of defects and long-range deformations in single crystals. Third-generation synchrotron radiation facilities like the ESRF create new experimental possibilities which are related to the high energy and the low emittance of the electron beam. In the case of the ESRF machine, the 6 GeV electron beam produces high-energy and high-flux X-ray beams (typically exploitable up to 120 keV at the D5 beam line). Thus, diffraction topographic investigations of heavy and/or bulky samples in transmission and real-time experiments at the 0.01 s time scale are feasible. The low emittance ($\simeq 10^{-10}$ m rad in the vertical plane) implies that the source size is relatively small (100–200 μm FWHM). Since the experimental station is relatively distant from the source (minimum 32 m), the 'geometrical' resolution of topographs, dS/D [S being the source size, D the source-to-sample distance and d the sample-to-detector (often film) distance], is greatly improved compared with the topographic stations at older synchrotrons. Physically, this means that in white-beam topography the radiation incident on the sample may be considered as a quasi plane (polychromatic) wave. Practically, the enhanced geometrical resolution allows observation of details in the topographs with an acceptable resolution (less than 10 μm) at distances as great as 1 m from the sample. The characteristics of the ESRF source, particularly its coherence, mean that the usual assumptions made for contrast interpretation in diffraction topography may no longer be valid.

Thus, the interaction of the incident beam with the crystal, and the propagation of the diffracted beam outside the crystal should be considered when analyzing the mechanisms of contrast formation.

In most of the published contrast-mechanism models the source is assumed to give an incoherent illumination of the sample and, in general, the propagation of the diffracted wave field from the crystal to the detector is neglected. In the case of an incident beam which is either polychromatic (white-beam topography), or monochromatic but divergent (Lang topography), the contrast is explained taking into account only diffraction processes inside the crystal. The diffracted intensity, which is an integrated intensity (image), is then considered to be the superposition of intensities produced by incoherent point sources at the entrance surface of the crystal (Carvalho & Epelboin, 1990). The propagation of the diffracted beam is neglected in the previous topographic set-ups because the image is recorded very close to the sample (1–2 cm in the laboratory techniques, about 10 cm on the previous synchrotron radiation topographic set-ups). This small sample-to-detector distance is necessary because of the rapid degradation of the spatial resolution when the film is moved away from the sample, this fact being associated with the relatively bigger source sizes and smaller source-to-sample distances. Whilst the ESRF topography configuration means that there may be no significant geometrical degradation of the image resolution, the evolution of the wavefields during

propagation to the detector may no longer be negligible. Effects due to the coherence of the incident beam are mainly visible at discontinuities in the refractive index (Cloetens, Barrett, Baruchel, Guigay & Schlenker, 1996). Since a dislocation displays a smooth variation of distortion at a scale of the order of the transverse coherence length of usual sources, the assumption of the incoherent point sources is justified. This explains the similarity between the synchrotron radiation topographs and laboratory traverse topographs in most of the cases. In the case of ESRF sources, where the transverse coherence length of the incident illumination is often much greater, this assumption may no longer be valid (Carvalho & Epelboin, 1990).

Tanner and co-workers have demonstrated in pioneering work that when using a synchrotron radiation source where the geometrical criterion is not resolution limiting, the direct image width of an edge dislocation may be observed to change with variations of the sample-to-film distance (Tanner, Midgley & Safa, 1977). This was explained as being due to the change of the beam divergence induced by the defect through orientation contrast. They concluded that the image width of an edge dislocation is sensitive to the sign of the Burgers vector. Unfortunately, problems with the beam stability prevented Tanner and co-workers from studying these effects in more detail, and the reported observations remained unique until the ESRF machine was ready. Therefore, in our experiments, we turned our attention towards the direct image of dislocations, and looked for contrast changes in shape and width as a function of the sample-to-film distance.

In addition, the plane-wave property has been used to compare simulated images of dislocations with experimental results obtained in monochromatic radiation as a function of the Bragg-angle offset of the sample. This is interesting from both a theoretical and a practical point of view, since the spatial resolution of defects in images can be greatly enhanced by using high angular offsets (weak-beam topography), but far from the peak of the rocking curve the diffracted photon flux is greatly reduced and hence one has a lower signal-to-noise ratio. Before describing the experimental procedures and presenting the results, we briefly recall the generally accepted models for the dislocation contrast in diffraction topography.

2. Description of dislocation contrast: width of the direct image

Contrast is considered to derive from the interaction between the incident and scattered beams and the deformed region associated with the defect. The scattering process may produce:

(i) A direct image (also called kinematical image), when the misoriented region can diffract other components in λ or θ of the white or divergent monochromatic incident beam with respect to those diffracted by the perfect matrix, and results in added intensity compared with the beam diffracted by the perfect matrix (Authier, 1967). Direct images thus give increased intensity (black with the usual printing conventions).

(ii) A dynamical image, which is associated with the screening effect that the defect induces in the propagation of the wave fields inside the Borrmann triangle, and to the creation of new wave fields in the highly deformed regions around the defect (Authier, 1967). Dynamical images give a decreased intensity (white) usually accompanied by a complex interference pattern which fills most of the Borrmann triangle. Let us note that these also include the intermediary images in Authier's notation.

Direct images provide a tool for studying the properties of the incident beam, since they originate directly from the defect without further dynamical propagation in the perfect matrix, which could complicate the interpretation. Any contrast change related to the coherent properties of the incident beam or to the sample-to-film distance, d, will modify the width of the direct image, V. This width is related to the distorted region around the dislocation core which is misoriented by $\pm x\omega_h$, where ω_h is the intrinsic reflection width and x is a parameter which has been measured to be between 0.5 and 2 for silicon (Miltat & Bowen, 1975), and which is considered as a small 'mosaic' crystal embedded in the perfect matrix (Authier, 1967). The order of magnitude for the image width of dislocations is

$$V_s \simeq (d_h/\pi x\omega_h)|\mathbf{h}.\mathbf{b}| \tag{1}$$

for a pure screw dislocation, $\mathbf{h}$ being the diffraction vector, $\mathbf{b}$ the Burgers vector and d_h the spacing of the corresponding Bragg planes, and

$$V_e \simeq 1.75V_s \tag{2}$$

for a pure edge dislocation (Lang, 1978). Both V_s and V_e are calculated normal to the dislocation line. In materials such as silicon or germanium, typical image widths are *ca* 10 µm or less for the low-order reflections at wavelengths of 1 Å. There are situations where the two misorientation contours $\pm x\omega_h$ are clearly separated, as sketched for the edge dislocation in Fig. 1(*a*). In this case, if the geometrical criteria are not resolution-limiting a double contrast may be observed (Fig. 1*b*) (Klapper, 1991; Authier & Petroff, 1964). The distance between the two maxima, L_0, calculated perpendicularly to the diffracted beam along the trace of the incidence plane, is (Authier, 1967)

$$L_0 = \left(\frac{1}{2\pi x\omega_h}\right)\left(\frac{1}{\cos\theta_B}\right) \times \left\{b_s\cos\beta\cos(\alpha+\theta_B)\cos(\alpha+2\theta_B)+\left[b_e\sin\beta \times \frac{2\cos(\alpha+\theta_B)\cos(\alpha+2\theta_B)+(1-2\nu)\cos\theta_B}{2(1-\nu)}\right]\right\} \tag{3}$$

where θ_B is the Bragg angle, α is the asymmetry angle, β is the angle between the direction of the dislocation and

the incidence plane, b_e and b_s are the edge and the screw components of the Burgers vector, and ν is the Poisson ratio. The double-contrast condition therefore offers the prospect of a direct determination of the Burgers vector modulus.

Since we are considering only scattering processes inside the crystal, the quantities V_s, V_e and L_0 are calculated at the exit surface of the crystal, so that we refer to them as belonging to the *intrinsic image width* of the dislocation.

3. Experimental techniques

The experiments were performed at the D5 'Optics' beamline at the ESRF. The size of the D5 bending magnet source is *ca* 0.4 mm FWHM horizontally and *ca* 0.3 mm FWHM vertically. The beamline has two experimental stations, the first located at *ca* 30 m and the second at *ca* 60 m from the source point. In such conditions we can expect a geometrical resolution of close to 1 µm or less if d = 10 cm. Retaining a good spatial resolution far from the sample is important since it simplifies the geometrical constraints for the sample environment (cryostats, furnaces, magnets *etc.*). The sample was a 0.325 mm thick Ge ($\bar{1}10$) crystal, with a low dislocation density. Since a high energy (> 50 keV) is required to achieve the direct image condition (μt < 1) for this sample, low $2\theta_B$ values are obtained for the studied reflections (less than 10°), thus allowing the films to be placed normal to the direct beam without significantly affecting the image width through projection effects. The use of high energies also drastically reduces the harmonic contamination due to the extended spectrum of the synchrotron radiation beam. The topographs were recorded on Kodak Industrex synchrotron radiation films (grain size 1–2 µm). Images were digitized from the films using a CCD camera (with linear intensity response) coupled to a microscope and the dislocation image width analysed using an image-analysis program. The widths were obtained from the half widths of the 'grey level' profiles measured perpendicularly to the dislocation line. In order to reduce the noise, the measurements were made on intensity profiles generated from projections of segments of the dislocation image parallel to the line vector. In the case of double contrast, the profiles were fitted with two Gaussian functions in order to determine the separation between the lobes. Great care was taken to keep the mean intensity level of the topograph constant, since the image width depends a little on the degree of film saturation. We estimate the overall error in the measured widths due to the recording and analysis methods to be *ca* 10%. The stability of the set-up was not a crucial point, since the exposure times were *ca* 0.5 s. The experimental results on the direct images are presented in §4.

Another series of experiments have been performed using monochromatic radiation on the same sample using a silicon monochromator in transmission geometry in an almost non-dispersive mode. Since silicon has intrinsic diffraction widths smaller than those of germanium for

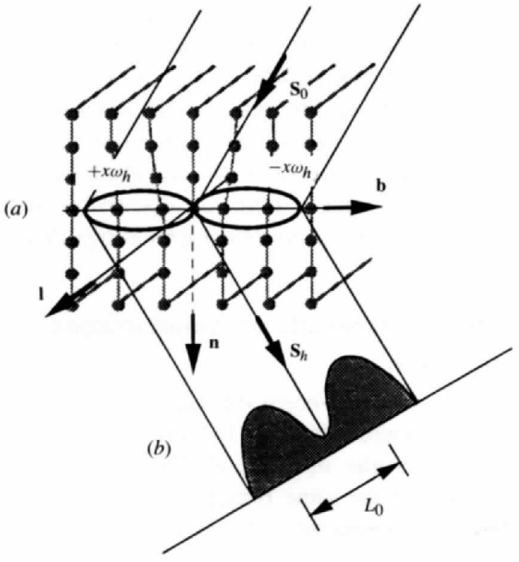

Figure 1
Explanation of the double contrast in direct images of dislocations. (*a*) The equal misorientation contours around an edge dislocation with **b** parallel to the surface. **b**, **n** and $\mathbf{S}_h$ indicate the directions of the Burgers vector, of the normal to the entrance surface and of the diffracted beam, respectively. (*b*) The qualitative distribution of the diffracted intensity.

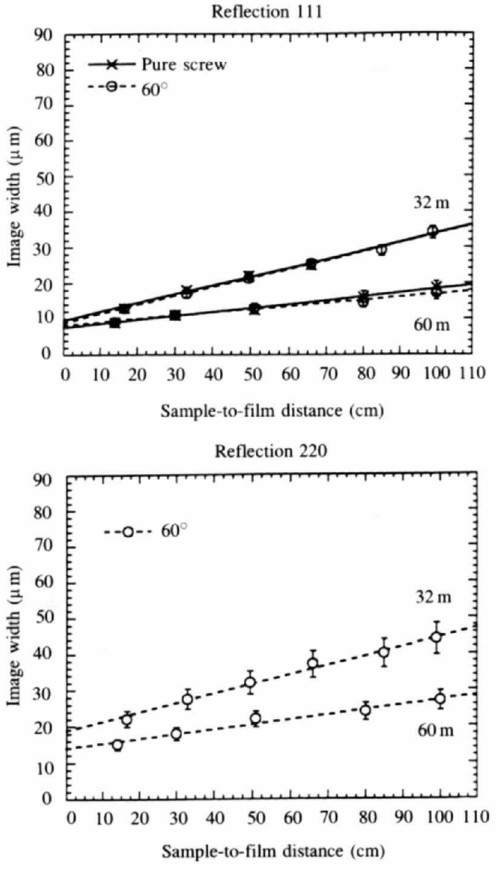

Figure 2
Image width of the dominant screw dislocations of Figs. 4(*a*) and 4(*b*) for the 111 and 220 reflections for both the orientations (see text). For reflection characteristics see Table 1.

the same reflection, the monochromatic beam behaves almost as a plane wave. Topographs were recorded on several points of the rocking curve of the Ge sample. The interpretation of the images has been carried out with the help of a simulation program written by one of us (YE) which considers the incident beam to be a monochromatic plane wave. A discussion about the experimental and simulated topographs is reported in §5.

4. Experimental results on direct images

4.1. *Image width*

Two series of white-beam topographs were recorded at two sample-to-source distances (32 and 60 m) as a function of the sample-to-film distance, d. The sample was set to diffract at almost the same Bragg angle in both cases, but rotated by 180° around the vertical axis in the second series, *i.e.* exchanging the entrance and exit surfaces. We refer to the first series (at 32 m) as topographs taken in the 'Π orientation', the second (at 60 m) as in the 'O orientation'. We could record images with an acceptable resolution up to 1 m from the sample. The perfect dislocations studied had Burgers vector 1/2⟨110⟩. Their straight segments typically lie along directions ⟨110⟩ at 0 or 60° to the Burgers vector

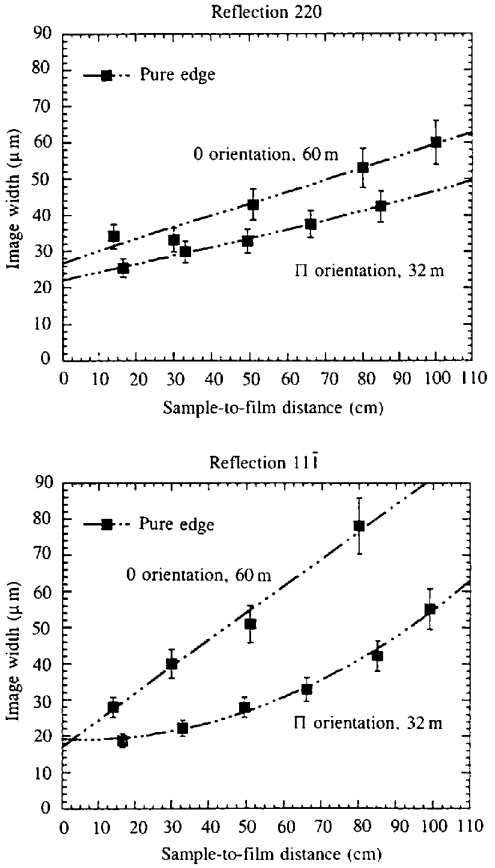

Figure 3
Image width of the dominant edge dislocations of Fig. 4(*c*) for the 220 and 11$\bar{1}$ reflections for both the orientations (see text). For reflection properties see Table 1.

owing to a low core energy for these orientations (Hull & Bacon, 1984). More rarely, pure edge dislocations were observed.

For all the dislocations studied the only contrast change observed with increasing d was an evolution of the image width, but the behaviour depends strongly on the type of dislocation, on the directions of the Burgers vector, **b**, and the dislocation line, **l**, with respect to the detector plane. Figs. 2 and 3 show the experimental image widths *versus* d for the pure screw, 60° and pure edge dislocations shown in Fig. 4 (for the vectors **b** and **l** see Table 1).

For a pure screw dislocation the image width increases linearly with d, more rapidly at 32 m than at 60 m and independently of the reflections studied. This difference therefore arises only from the different source-to-sample distances and not from the deformation around the dislocation core, and implies that it is a direct effect of the angular size of the source, Ω_s. This is not surprising since the helicoidal deformation associated with a screw dislocation along the line **l** does not significantly affect the divergence perpendicular to **l**.

More surprising is the similarity in the behaviour between the 60° and the screw dislocations, since the edge component may, in principle, perturb the incoming beam divergence. We believe that this unchanged behaviour is connected with the magnitude of the projection of the edge component perpendicular to the dislocation line in the detector plane, $\mathbf{b}_\perp$, which is negligible in this case. This means that the strain field of the 60° dislocation, as seen by the beam, closely resembles that of the pure screw (Fig. 5).

$\mathbf{b}_\perp$ is not negligible for the pure edge dislocation, which shows a completely different behaviour. Now the general trend depends mainly on the crystal orientation (O or Π) and on the reflection rather than on the source-to-sample distance. We explain such behaviour as a change of the beam divergence produced by the projection $\mathbf{b}_\perp$ in the same way as proposed by Tanner *et al.* (1977). This change may result in a higher or lower slope of the fits if this component adds or subtracts divergence to the beam.

The best fit of most of the experimental data is obtained using a linear fit $V + \Omega_s d$ (where V is the intrinsic image width, *i.e.* the width at the exit surface of the crystal). This may be due to the fact that the dislocation is not a 'Gaussian' object.

The slope of the linear fit in the case of a pure screw dislocation may be used to estimate the source size. In our case, taking $\Omega_s \simeq 10$ μrad at 60 m we calculate a horizontal source size of *ca* 0.6 mm since the dislocation studied had their line vector oriented approximately perpendicular to the orbital plane, a value which is in reasonable agreement with previous measurements (0.4 mm FWHM).

Comparison of the extrapolated values of V with those calculated from equations (1) and (2) (see Table 1) gives a fairly good agreement with the theoretical image width when the value of x is between 0.5 and 1.5, *i. e.* we obtain the predicted values apart from a simple broadening term due to the angular size of the source. This remains true

Table 1
Calculated [from equations (1) and (2) for $x = 1$] *versus* experimental values at $d = 0$ for the image width for the examined dislocations.

Dislocation	l	b	Reflection	Orientation	$V_{s.c}$ (μm)	V_{exp} (μm)
Pure screw	[011]	1/2[011]	111 $\lambda \simeq 0.23$ Å	O	9	7.5
			111 $\lambda \simeq 0.24$ Å	Π	9	9.5
60°	[101]	1/2[011]	111 $\lambda \simeq 0.23$ Å	O	9*	8
			111 $\lambda \simeq 0.24$ Å	Π	9*	8.5
			220 $\lambda \simeq 0.17$ Å	O	10*	14
			220 $\lambda \simeq 0.18$ Å	Π	9*	18.5
Pure edge	[011]	1/2[01$\bar{1}$]	220 $\lambda \simeq 0.17$ Å	O	17	26.5
			220 $\lambda \simeq 0.18$ Å	Π	16	21
			11$\bar{1}$ $\lambda \simeq 0.23$ Å	O	16	17
			11$\bar{1}$ $\lambda \simeq 0.24$ Å	Π	15	19†

* Value for the screw case. † Value obtained by fitting results with quadratic function.

even for the pure edge dislocation, for which the image width often does not increase linearly for reasons which are discussed in §4.3. In this case the values at zero distance are more difficult to determine due to the quality of the fitting procedure. However, it is found that the measured widths in the two orientations seem to converge to a common value (see Table 1). Again, the extrapolated values at $d = 0$ are in fair agreement with the theoretical ones.

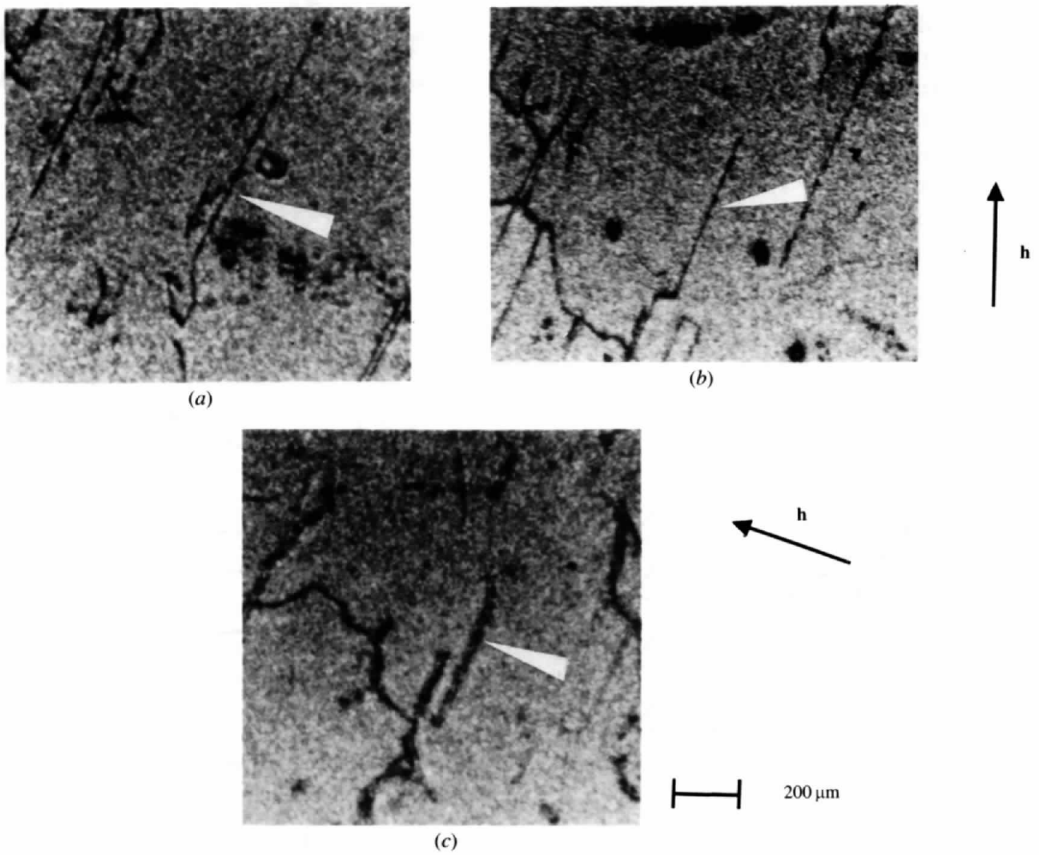

Figure 4
Topographs of the investigated dislocation: (*a*) pure screw dislocation; (*b*) the 60° dislocation; (*c*) dominant edge dislocation. The reflections are: 111 for (*a*) and (*b*), and 11$\bar{1}$ for (*c*) (see Table 1 for characteristics of the reflections).

4.2. *The focusing/defocusing effect*

In the case where $\mathbf{b}_\perp$ is maximized ($\mathbf{b}_\perp \simeq \mathbf{b}$), the contrast change when changing from the O to the Π orientation can be rather spectacular. Figs. 6(*a*) and 6(*b*) show what we call the 'focusing/defocusing' effect in the image of the dislocation marked by the arrow in the 220 topographs recorded at 50 cm from the sample. The dislocation of Burgers vector 1/2[110] is composed of three segments *A*, *B* and *C*, running roughly parallel to the directions [111], [110] and [11$\bar{1}$], respectively. The contrast of segments *A* and *C* changes from double to single type and *vice versa* when changing from orientation O to orientation Π, whereas the contrast of segment *B* remains unchanged. This effect can be explained by noting that the $\mathbf{b}_e$ component changes sign with respect to the dislocation line between *A* and *C*, and is zero along segment *B* (Fig. 6*c*). This sensitivity to the sign of the edge component of the Burgers vector is such that when the sign is positive the separation of the lobes is visible through orientation contrast, and when the sign is negative the deformation 'focuses' the beam and single contrast is observed (Fig. 7), the contrast remaining unchanged for segment *B* because of its pure screw character. The focusing/defocusing behaviour is confirmed when we plot the image width of the three segments *versus d* for the orientation of Fig. 6(*a*) (Fig. 6*d*). The width of segment *A* increases rapidly as a function of *d*, that of segment *C* shows a slight minimum around d = 50 cm, and segment *B* behaves in the same way as the dominantly screw dislocations as analysed before. An extrapolation of these results to zero distance leads to an image width for segment *A* very close to the one observed for segment *C*, as could be expected since in this reflection the two segments are almost equivalent from the point of view of the intrinsic image.

The analysis of the double contrast *versus d* also provides a means of determining the parameter x in equation (3), and hence allows the estimation of the modulus of **b**, which for X-rays is usually carried out by analysis of section topographs (Epelboin, 1985).

As an example, for the 220 reflection (θ_B = 2.47°, α = 0), equation (3) simplifies to

$$L_0 \simeq (b/4\pi x\omega_h)[\cos\beta + 2.9\sin\beta], \qquad (4)$$

since $\nu \simeq 0.27$ for germanium, $b_s = b\cos 60°$ and $b_e = b\sin 60°$. For our geometry, the expression inside the

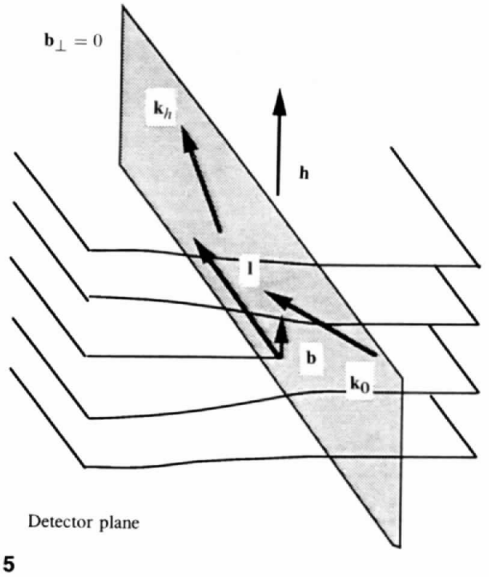

Figure 5
Geometrical situation where $\mathbf{b}_\perp = 0$. In this case the 'edge'-type distortion around the dislocation core does not perturb the beam divergence.

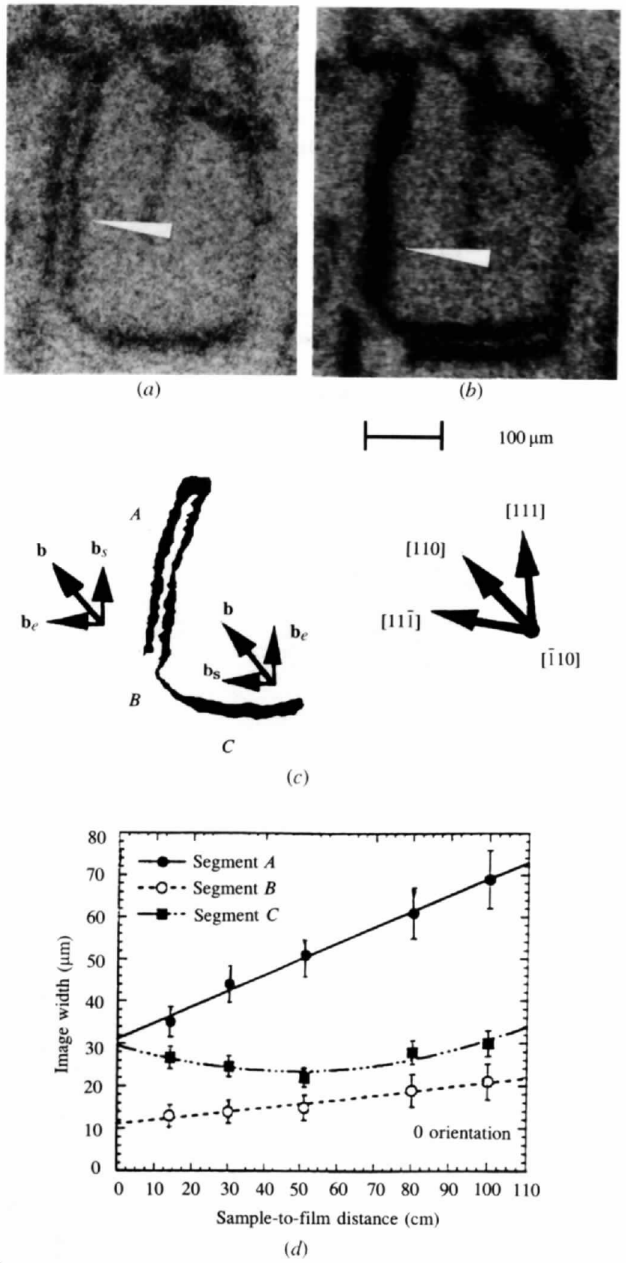

Figure 6
'Focusing/defocusing' effect for the dislocation segment marked by the arrow when going from (*a*) the O orientation (λ = 0.19 Å) to (*b*) the Π orientation (λ = 0.18 Å); 220 reflection (for reflection characteristics see Table 1). (*c*) The geometrical explanation of the contrast change (see text). (*d*) The image width *versus* the distance *d* for the three segments (Barrett, Baruchel, Härtwig & Zontone, 1995).

square brackets is ~3, so that the modulus of **b** is

$$b \simeq 4.2x\omega_h L_0. \quad (5)$$

Fig. 8 shows the lobe separation as a function of d for segment A in the topograph of Fig. 6(a). A linear fit allows estimation [using (5)] of the intrinsic separation L_0 from the interpolated value at zero distance, and the parameter x from the slope $4x\omega_h$, since each side of the dislocation misoriented by $x\omega_h$ with respect to the perfect matrix adds a divergence $2x\omega_h$ to the diffracted beam. The linear fit gives $L_0 \simeq 16\,\mu$m and the slope $\simeq 28\,\mu$rad, so that $x \simeq 1$ since $\omega_h = 6.5\,\mu$rad. Neglecting projection effects in the measurements we calculate $b \simeq 4.4$ Å, which differs by 10% from the theoretical value (4 Å).

4.3. *Uncertainties in the determination of x*

The simple analysis of the double-contrast evolution *versus d* in direct images gives a method for measuring the modulus of the Burgers vector for an edge dislocation *via* the calculation of the x parameter. Two main phenomena may give uncertainties in the x value calculated from the double-contrast separation *versus d*.

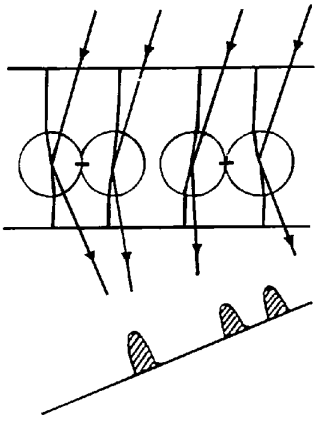

Figure 7
Geometrical explanation of the single and double contrast for an edge-type dislocation (Miltat, 1980).

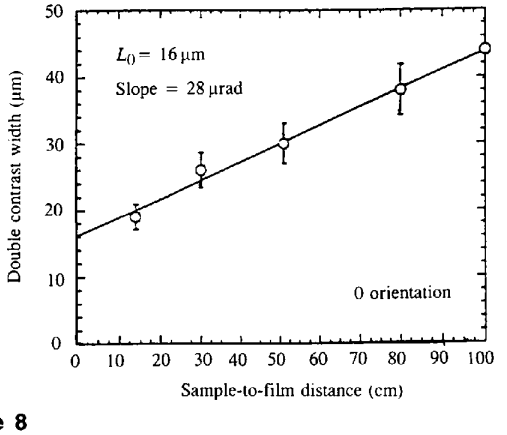

Figure 8
Separation of the lobes *versus* the distance d for the dislocation part A of Fig. 5(a) for the 220 reflection.

The first concerns the 'white' extended spectrum of the synchrotron radiation sources. Fig. 9 shows the measured image width of the 60° dislocation as a function of wavelength. At longer wavelengths the image width does not decrease continuously but jumps to higher values when the contribution of the harmonic becomes dominant. This can be a serious problem when using white-beam illumination, since some filtering is always necessary in order to keep a low heat load on the sample during the exposure time. This cuts out the longer wavelengths and hence enhances the harmonic contribution. The harmonic content can therefore modify the apparent value of x.

Another source of errors may, in principle, derive from the transmission geometry itself, since it adds a supplementary divergence $2\omega_h$ (in the symmetrical case) in the diffraction plane because of chromatic aberration (Brauer *et al.*, 1995). At longer wavelengths where the direct images are narrower, this contribution can exceed the intrinsic source divergence and hence may cause an important loss of resolution in the diffraction plane.

The experimental observation of this chromatic aberration is not easy since it is difficult to simultaneously find dislocations aligned parallel and normal to the diffraction plane in the same reflection. We have tried to estimate this effect through the single- and double-contrast analysis *versus d*. In the previous calculations it was assumed that the double contrast depends principally upon the misorientation of the Bragg planes. However, more rigorously, the total image width will depend also on the divergence of the incoming beam. Figs. 10(a) and 10(b) show the results for segment C of the dislocation of Fig. 6 for the 111 and 220 reflections. Since in the 111 reflection this segment is perpendicular to the diffraction plane and the intrinsic diffraction width ω_h is quite large ($\simeq 12\,\mu$rad), we expect the slope of the image width as a function of d to be larger than the double-contrast image slope. For the 220 reflection, for which ω_h is only 7 μrad and the diffraction plane is at *ca* 45° with respect to the dislocation line, we should observe similar behaviour for both features. This seems to be confirmed qualitatively by the plots of Fig. 10, but a

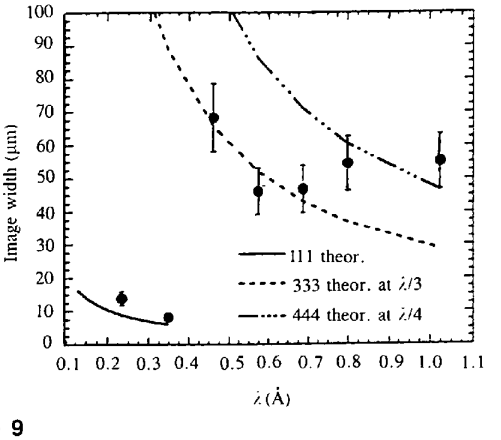

Figure 9
Experimental and theoretical image widths as a function of wavelength for the 60° dislocation of Fig. 4(b).

quantitative inspection of the gradients suggests another interpretation.

Indeed, if we assume that the double contrast depends only on the misorientation of the Bragg planes and the image width also on the beam divergence, we calculate a beam divergence of *ca* $4.5\omega_h$ for the 111 reflection (Fig. 10*a*), and $2\omega_h$ for the 220 reflection (Fig. 10*b*). This is the reason why we observe a defocusing effect, when changing the orientation, only for the 220 reflection, the misorientation measured from the double contrast being $4\omega_h$ for the 111 reflection and $3\omega_h$ for the 220 reflection. Here we neglect the intrinsic source divergence (the angular source size) because it is always less than 10 μrad.

In conclusion, we have one case which is in agreement with the supposed $2\omega_h$ diffracted beam divergence and another one which differs by a factor of two from this value. The reason for the higher beam divergence for the 111 reflection can be explained by the fact that we are actually looking at the beam diffracted by a defect, which is in principle not related to the perfect crystal matrix. In §2 we have seen that the intensity of the direct image depends on the volume of the crystal which is misoriented by $\pm x\omega_h$, $x \simeq 1$, with respect to the perfect matrix. In the white beam all the regions inside the misorientation contours $\pm 1\omega_h$, $\pm 2\omega_h$, ... are excited, but the volume, and thus the diffracted intensity, decreases with the square of $1/x$. The region $\pm 2\omega_h$, which still carries a significant amount of intensity, may extend the direct image observed far from the sample because of the orientation contrast: the centre of gravity of the lobes will vary only slightly, but the total image width can be larger. Such a reason could explain even the non-linear behaviour of the pure edge dislocation observed in the $11\bar{1}$ reflection. This does not apply for the 220 reflection, because the $\pm\omega_h$ contour is larger, ω_h being smaller, hence even far from the sample this contour dominates the image formation.

So far, no definitive interpretation can be found at the moment in our measurements, since the error in the slope is too large ($\simeq$ 10 μrad), but we expect some improvement in the experimental results when the ID19 'Topography and High-Resolution' beamline is ready, since the intrinsic source divergence is much smaller ($\simeq$ 1 μrad) (Baruchel, Draperi & Zontone, 1993).

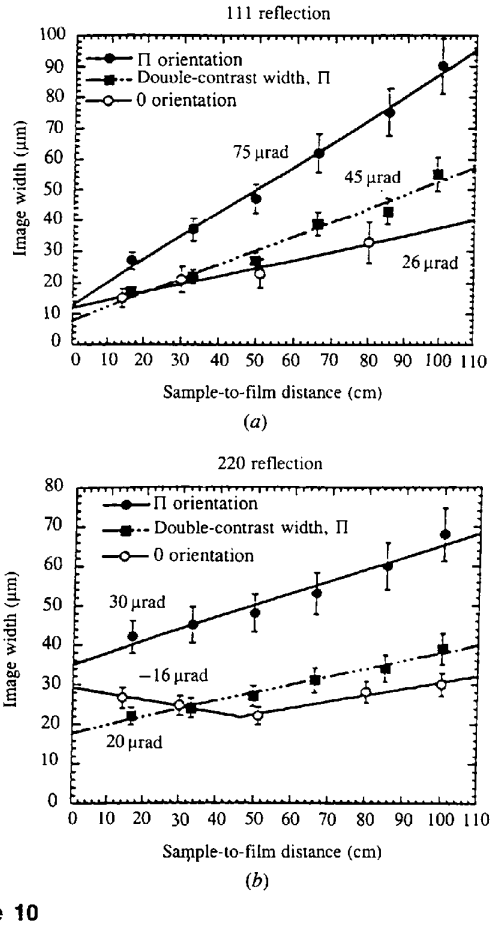

Figure 10
Image widths and double-contrast widths for the segment *C* of the dislocation of Fig. 5(*a*) as a function of the distance *d* for (*a*) the 111 reflection, and (*b*) the 220 reflection for both the crystal orientations (O and Π) (for reflection characteristics see Table 1).

4.4. *Contrast along the dislocation line*

The high geometrical resolution of the ESRF sources and the possibility of analysis of the contrast variation with *d* help to explain the contrast which is sometimes observed along the dislocation line. Fig. 11 shows the 'fraying' of a screw dislocation image when observed far from the sample. The image variations, due to the orientation contrast, can be explained by the presence of other defects close to the dislocation which distort the Bragg planes perpendicular to the dislocation line (as does the defect *D* in the region indicated by the arrow in Fig. 11). The misorientation can therefore be measured (± 25 μrad in the example) and information could be extracted about the interaction between defects.

Another example is shown in Fig. 12, where a pronounced dot character appears along an edge dislocation at increasing values of *d*. Since the number of dots varies as a function of *d* we think that the contrast change could be attributed to the overlapping of very divergent beams coming from highly misoriented regions ('precipitates') near the dislocation core, *i.e.* the dislocation is probably 'decorated' with segregation defects (Van Bueren, 1960).

5. Double-crystal topography

5.1. *Dislocation images recorded near to the peak of the rocking curve*

It is well known that the contrast in monochromatic beam topography is related to the geometrical property of the incident beam which can produce either a spherical or a plane wave. We expect to be in a plane-wave condition when $\omega_h >> \Omega_e$, where Ω_e is the effective divergence of the beam measured from the base of the Borrmann triangle. In particular, for the symmetrical case $\Omega_e \simeq 2t \sin\theta_B/D$, t being the crystal thickness (Carvalho & Epelboin, 1990). Since D is very large at the ESRF topographic stations, Ω_e

can easily be as small as 1 μrad. This justifies the 'almost plane-wave' assumption. Several 111 topographs of the Ge crystal have been recorded using the 111 reflection from a Si monochromator in Laue geometry at $\lambda \simeq 0.17$ and 0.35 Å. The experimental images have been compared with simulated ones. A complete description of the program and the method used to simulate straight dislocations in X-ray topographs can be found in a review paper by Epelboin (1985). In particular, the contrast variations and width of dislocation images for different working points on the Ge rocking curve were studied. Figs. 13(*a*) and 13(*b*) show the experimental and simulated images of the dislocation of Fig. 4(*b*) recorded at the peak of the Ge rocking curve for the chosen wavelength. They display a

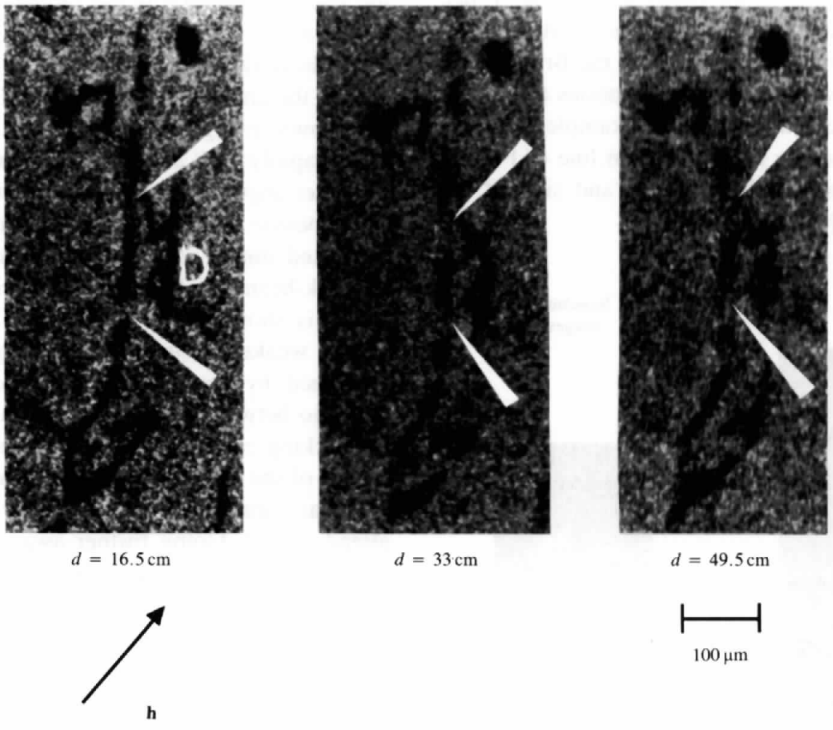

Figure 11
The 'fraying' of part of the screw dislocation image at different sample-to-film distances *d*. The reflection is the 111 (see Table 1). The effect is seen through orientation contrast due to the distortion induced by the defect *D* (see arrows).

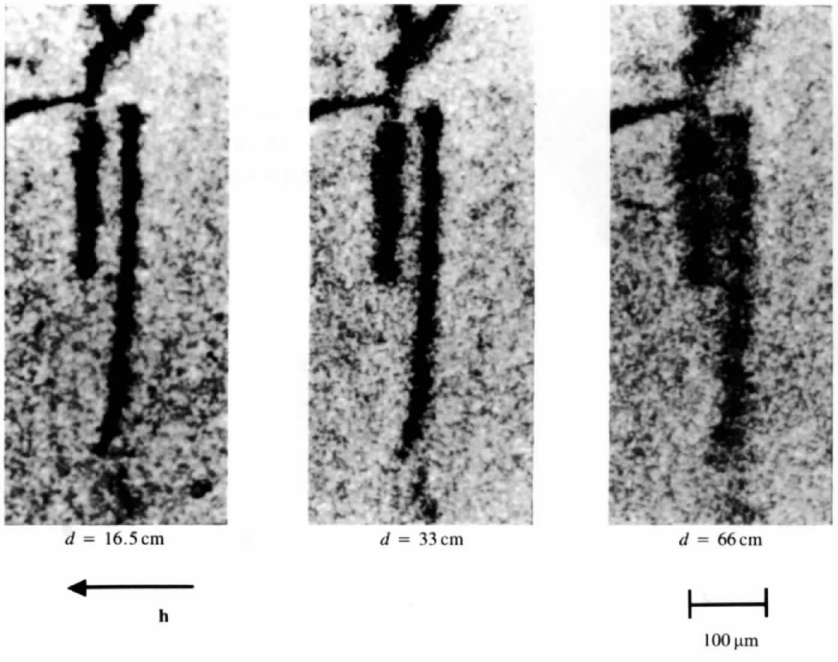

Figure 12
The $11\bar{1}$ topograph of the edge dislocation for different sample-to-film distances *d*. Note the pronounced dot character at increasing values of *d*.

complex dashed pattern which is due to the dislocation being inclined relative to the crystal surface and arises from 'beating' of the wave fields with a period given by the *Pendellösung* length. This is confirmed by the variation of the periodicity of the fringes when we change the working wavelength. We can see that this complex pattern is very well reproduced by the simulations. In particular, the non-homogenous character of the topograph of Fig. 13(*b*), which is due to a small bending, has been simulated by taking into account a small departure from the Bragg angle (2 μrad). Comparison with computer simulations allows the strain field to be fully characterized. For example, from the white–black sequence along the dislocation line of Fig. 13 it was possible to establish the modulus and sign of the Burgers vector (+1/2 [011]).

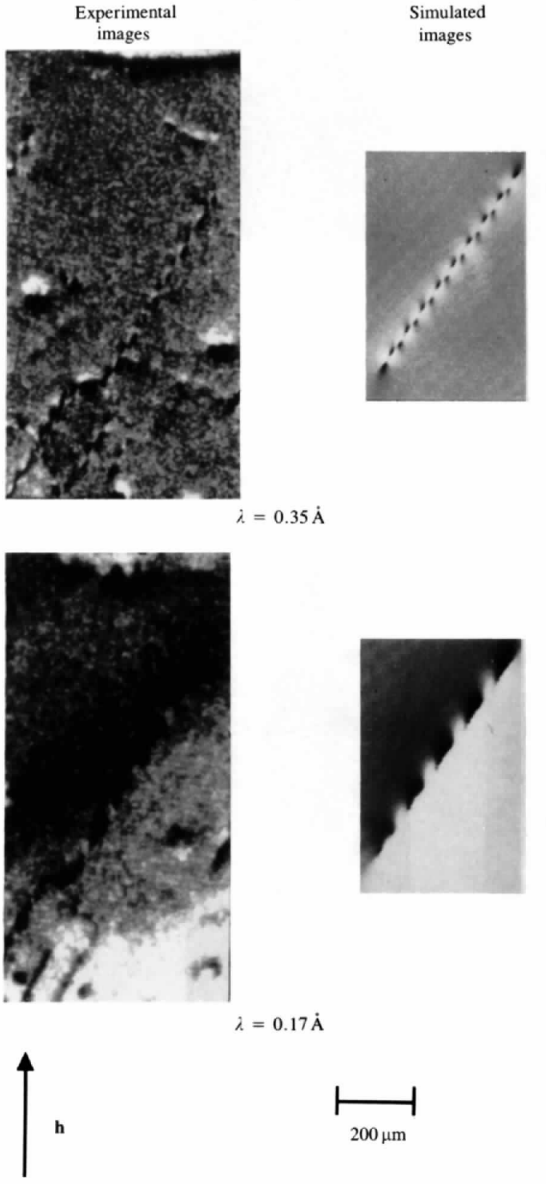

Figure 13
111 experimental and simulated topographs of the dislocation of Fig. 4(*a*) near to the peak of the Ge rocking curve at $\lambda = 0.35$ Å and $\lambda = 0.17$ Å.

5.2. *Dislocation image width in the 'weak-beam' case*

One interesting aspect of monochromatic beam topography is that the spatial resolution can be enhanced if we record the topographs on the tails of the rocking curve of the sample ('weak-beam' topography). This happens because only the deformed regions close to the core of the defect are in the Bragg position so that the images are very thin, the spatial resolution being limited by the detector and by the signal-to-noise ratio.

We have therefore measured the image width as a function of the angular offset from the Bragg peak. The results are shown in Fig. 14. They indicate that the image width drops rapidly until about ω_h and then decreases very slowly at higher angular offset, the contrast becoming weaker and the exposure time longer. This trend is confirmed by the simulated image width as shown in Fig. 14. An example of weak-beam topography and the corresponding simulated image is shown in Fig. 15.

The weaker contrast at high angular deviations can be explained by considering a simple model. We consider the ratio between two Lorentzian functions assumed to be the rocking curves of the perfect matrix and the reflecting region of the dislocation, whose centres differ by ω_h. This ratio has a maximum at *ca* $3/2\,\omega_h$ where the image width is already small. Going further away will therefore result in longer exposure times and lower signal-to-noise ratios with no significant enhancement of the spatial resolution.

We note that the simulated image in 'weak beam' at 36 keV still has a dashed character which is not observed on the topograph. The dashed character of the simulated image arises from the dynamical image. Since the dislocation is inclined inside the crystal it creates a set of fringes which are visible, near the black-line image corresponding to the misoriented region near the core of the dislocation which fulfills the Bragg condition ('weak-beam' image), in the simulations. It is blurred in the experiment.

The discrepancy between the experimental and simulated values is attributed to a blurring effect associated with the sample-to-film distance (≃ 13 cm), the grain size of the synchrotron radiation films (2–3 μm), the residual divergence,

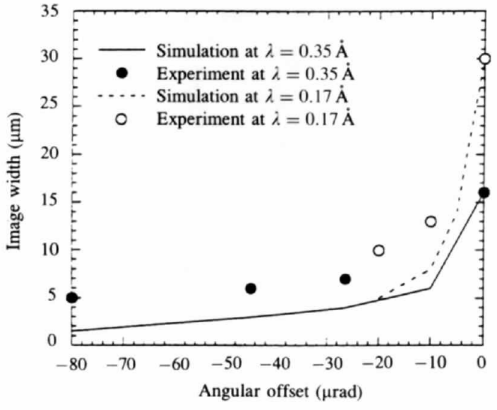

Figure 14
Experimental and simulated image width as a function of the Bragg-angle offset for the 60° dislocation; 111 reflection.

the limited spatial resolution of the films, and the finite band pass of the incoming beam and background intensity levels. The factors are thought to combine to reduce the visibility of the finely spaced (5–6 μm) fringes.

6. Conclusions

The results presented show that the propagation out of the crystal of the beam diffracted by the strained regions around a defect should be taken into account in order to explain the direct image width of the dislocations. The simple analysis of the direct images as a function of the sample-to-film distance allows:

(i) identification of the character of the dislocation;

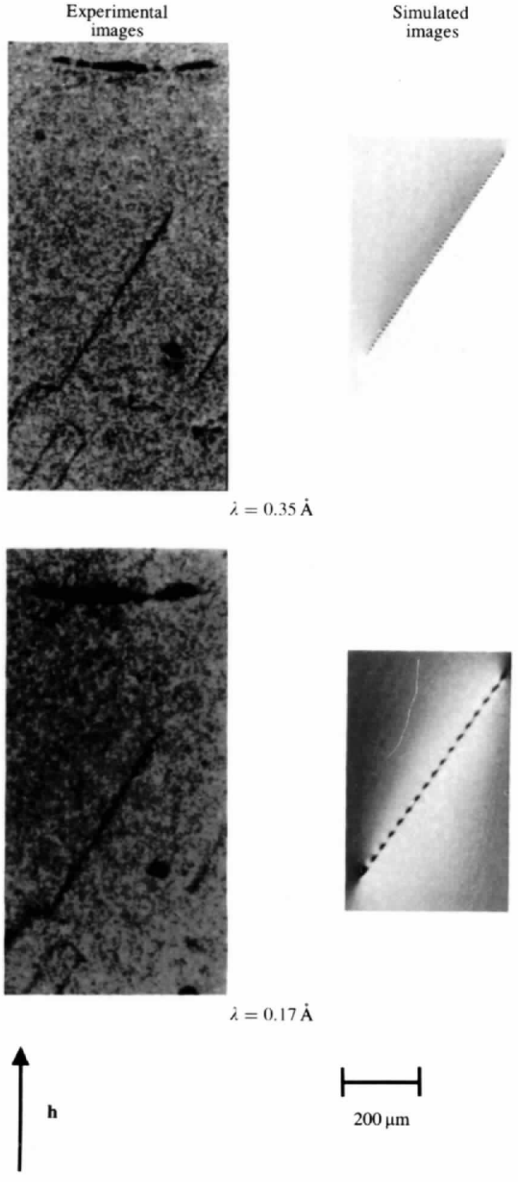

Figure 15
111 experimental and simulated topographs of the dislocation of Fig. 4(*a*) in the weak-beam condition at $\lambda = 0.35$ Å (Bragg-angle offset: 60 μrad) and at $\lambda = 0.17$ Å (Bragg-angle offset: 17 μrad).

(ii) determination of the sign of the Burgers vector of a non-screw dislocation;

(iii) in favourable conditions, calculation of the modulus of the Burgers vector of a non-screw dislocation.

This analysis demonstrates that the high collimation of the X-ray beams of third-generation synchrotron radiation sources enhances the potential of topographic investigations. When it is possible to extrapolate the image width at zero distance the results are substantially in agreement with the presently accepted theory.

In these studies, no absolute evidence of contrast changes in direct images at high values of d have been observed which could be related to the large coherence width of the ESRF beams together with the change of propagation direction as a function of λ as proposed by Carvalho & Epelboin (1990). In §4.2 we discussed the appearance of the double contrast as produced by a 'defocusing' effect and not by a coherent effect. The fact that it is easier to observe the double contrast at shorter wavelengths tends to confirm this hypothesis. This is not a definitive answer on this subject, however, since the coherence width in our experiments was perhaps too small (< 3 μm). A more precise analysis will be possible at the ID19 'Topography and High-Resolution Diffraction' beamline, where the coherence width is five times higher because of the larger source-to-sample distance (145 m). In addition, the tunability of the wiggler source will permit the use of higher wavelengths without excessive harmonic contamination.

For experimental observation in a monochromatic beam, the simulations based on the plane-wave approximation are in close agreement with the experimental results both on the peak and on the tails of the rocking curve, and in our case appear to confirm the almost plane-wave character of the ESRF beams. Since plane-wave images are rather easy to simulate, it means that quantitative analysis of defects might be easily made at the ESRF using monochromatic experiments together with simulations.

The authors would like to thank B. K. Tanner for very helpful discussions about the image width of dislocations in 'weak-beam' topography. They are also very grateful to A. K. Freund, who gave us the possibility of performing our experiments at the D5 beamline, and to the other colleagues of the Topography Group, especially E. Prieur, P. Cloetens and P. Rejmánková, for their help during the experimental work.

References

Authier, A. (1967). *Adv. X-ray Anal.* **27**, 9–31.
Authier, A. & Petroff, J. F. (1964). *C. R. Acad. Sci.* **259**, 4238.
Barrett, R., Baruchel, J., Härtwig, J. & Zontone, F. (1995). *J. Phys. D*, **28**, A250–255.
Baruchel, J., Draperi, A. & Zontone, F. (1993). *J. Phys. D*, **26**, A9–14.
Brauer, S., Stephenson, G. B., Sutton, M., Mochrie, S. G. J., Dierker, S. B., Fleming, R. M., Pindak, R., Robinson, I. K., Grübel, G., Als-Nielsen, J. & Abernathy, D. L. (1995). *Rev. Sci. Instrum.* **66**(2), 1506–1509.

Carvalho, C. A. M. & Epelboin, Y. (1990). *Acta Cryst.* A**46**, 449–459.
Cloetens, P., Barrett, R., Baruchel, J., Guigay, J. P. & Schlenker, M. (1996). *J. Phys. D.* **29**, 133–146.
Epelboin, Y. (1985). *Mater. Sci. Eng.* **73**, 1–43.
Hull, D. & Bacon, D. J. (1984). *Introduction to Dislocations.* Oxford: Pergamon.
Klapper, H. (1991). *Crystals*, Vol. 13, *X-ray Topography of Organic Crystals.* Berlin: Springer-Verlag.
Lang, A. R. (1978). *Diffraction and Imaging Techniques in Materials Science.* Amsterdam: North Holland.
Miltat, J. (1980). *Characterisation of Crystal Growth Defects by X-ray Methods.* New York/London: Plenum Press.
Miltat, J. & Bowen, D. K. (1975). *J. Appl. Cryst.* **8**, 657–669.
Tanner, B. K., Midgley, D. & Safa, M. (1977). *J. Appl. Cryst.* **10**, 281–286.
Van Bueren, H. G. (1960). *Imperfection in Crystals.* Amsterdam: North Holland.